Formation and dynamics of bubbles in breaking waves: Part II. The evolution of the bubble size distribution and breakup/coalescence statistics

By W. H. R. Chan, M. S. Dodd, P. L. Johnson, J. Urzay and P. Moin

1. Motivation and objectives

Breaking waves in oceans generate bubbles over a wide range of scales—an observation that has been replicated experimentally (Blenkinsopp & Chaplin 2010; Deane & Stokes 2002) and numerically (Wang et al. 2016; Deike et al. 2016; Chan et al. 2018a). The effects of these bubbles on the atmosphere and oceanic environment have motivated efforts to better understand the physical mechanisms behind the formation of this wide range of bubble sizes, which necessarily involve breakup and possibly coalescence events. This brief is the second part of a two-brief series documenting the current status of this investigation: in the first brief (Chan et al. 2018b), algorithms to identify bubbles and to detect bubble breakup and coalescence events in a two-phase simulation with knowledge of the volume fraction field are detailed. In this brief, these algorithms are used to characterize the evolution of the bubble size distribution in an ensemble of simulations of breaking waves, including the identification of breakup and coalescence events. Then, on the basis of trends observed in the evolution of the distribution and accompanying events, a pathway for the identification of potential mechanisms for bubble breakup and coalescence is outlined.

The contents of this brief are structured as follows: in Section 2, the ensemble of simulations of breaking waves introduced by Chan et al. (2018b) is described in greater detail, together with a discussion of the key scales involved in the analysis of breaking waves. In Section 3, the time evolution of the bubble size distribution computed from the aforementioned breaking wave simulations is discussed. In Section 4, the population balance equation is introduced in order to provide a framework for interpreting the evolution of the size distribution. In Section 5, some of the breakup and coalescence terms in the population balance equation are computed from the aforementioned simulations. Closing remarks on the identification of a potential set of bubble breakup and coalescence mechanisms on the basis of these computed statistics are offered in Section 6.

2. Breaking wave parameters and scales

In this work, an unstructured node-centered geometric unsplit volume-of-fluid-based incompressible two-phase flow solver with consistent mass and momentum advection developed by CTR and Cascade Technologies (Kim *et al.* 2014) was used to perform an ensemble of 30 simulations of breaking third-order Stokes water waves in air. A description of this ensemble was provided by Chan *et al.* (2018a,b), but will be reproduced

here with additional explanations for ease of reference. Parts of the subsequent discussion are also adapted from the publication by Chan et al. (2018a). Using the wavelength L as the characteristic length scale, and the corresponding deep water wave velocity $u_L = \sqrt{gL/2\pi}$ as the characteristic velocity scale corresponding to this length scale, the Weber and Reynolds numbers of the wave may be defined as $We = We_L = \rho_l u_L^2 L/\sigma$ and $Re = Re_L = \rho_l u_L L/\mu_l$, respectively. Here, ρ_l , μ_l , and σ respectively denote the density and viscosity of water, and the surface tension of the water-air interface. The Weber number characterizes the importance of inertial effects relative to capillary effects, while the Reynolds number characterizes the importance of inertial effects relative to viscous effects. The aforementioned simulations were performed for a wave with $We = 1.6 \times 10^3$ and $Re = 1.8 \times 10^5$. These parameters correspond to a 27-cm-long water wave at atmospheric conditions. The computational mesh consisted of about 4.2 million mesh nodes, the minimum grid spacing was L/216—equivalent to 1.25 mm at atmospheric conditions—and the length of the computational domain along each Cartesian axis was L. The mesh is nonuniform and is coarser closer to the edges of the domain in the wavenormal direction, such that a large majority of the generated bubbles are resolved with the minimum grid spacing. The initial wave steepness, which is the product of the wave amplitude and the fundamental wavenumber $2\pi/L$, was 0.55, and the corresponding initial velocity field was documented by Iafrati (2009). Periodic boundary conditions were employed in the directions parallel to the interface, and slip boundary conditions were employed in the wave-normal direction. For an illustration of what the wave looks like at the beginning and some time after it has broken, refer to Figure 7 of Chan et al. (2017) or Figure 13 of Chan et al. (2018a). Note that the characteristic velocity scale, and thus the dimensionless parameters We and Re, is defined differently by Chan et al. (2017).

To determine the relative importance of inertial, viscous, and capillary effects at a particular bubble size, it is instructive to consider the scales at which two of these effects are approximately equally important, nondimensionalized by the wave (integral) scales L and u_L . Consider, first, the balance of inertial and capillary effects. Hinze (1955) considered the case of sufficiently low concentration of the dispersed (gas) phase such that coalescence events are rare, and sufficiently large Reynolds numbers such that the smallest turbulent eddies in the continuous (liquid) phase are much smaller than the largest entities of the dispersed phase, so viscous effects are not dominant for these large entities. Hinze postulated that in this limit, the dominance of inertial forces due to turbulent fluctuations over capillary forces results in the fragmentation of large cavities and bubbles of the dispersed phase. A similar argument was brought forward by Kolmogorov (1949). For this to occur, the characteristic hydrodynamic pressure fluctuations $\rho u_{L_n}^2$ associated with velocity fluctuations of magnitude u_{L_n} at a characteristic length scale \ddot{L}_n will need to exceed the capillary pressure σ/D_{L_n} associated with a bubble of size D_{L_n} . If one assumes that a bubble is most likely acted upon by a turbulent eddy of the same size, then $D_{L_n} = L_n$. A physical justification for this assumption was offered by Hinze (1955) and refined by Chan et al. (2018a). Then, one may express the postulate above as $We_{L_n} > 1$, where We_{L_n} denotes the following Weber number

$$We_{L_n} = \frac{\rho_l u_{L_n}^2 L_n}{\sigma}. (2.1)$$

This postulated fragmentation cascade begins approximately at the integral scale ($L_n = L$) and is terminated at what has now been termed the Hinze scale ($L_n = L_H$), where the two forces above are balanced and $We_{L_H} \sim 1$. Suppose, in addition, that the turbulent

flow field in the mixed-phase region is approximately locally isotropic. Then, one could adopt the Kolmogorov scalings (Kolmogorov 1941, 1962) typically associated with the inertial subrange of isotropic turbulence. In particular,

$$u_{L_n}^2 \sim (\varepsilon L_n)^{2/3},\tag{2.2}$$

where ε is the average rate of dissipation and $L \gg L_n \geq L_H$. Then, one may rearrange Eqs. (2.1) and (2.2) to obtain, for $We_{L_H} \sim 1$,

$$L_{\rm H} \sim \left(\frac{\sigma}{\rho_l}\right)^{3/5} \varepsilon^{-2/5}.$$
 (2.3)

One could further assume that the characteristic dissipation rate is determined by the energy-containing scales, so in the case of a breaking wave, $\varepsilon \sim u_L^3/L = g^{3/2}L^{1/2}/(2\pi)^{3/2}$. Note that the length scale that enters the dissipation rate scale should technically be a function of the wave height from energy considerations, but for wave slopes of order 0.1 to 1, this distinction does not significantly impact this derivation. Substituting this expression for the dissipation rate into Eq. (2.2), and nondimensionalizing $L_{\rm H}$ with L, yields the nondimensional Hinze scale [see, also, Shinnar (1961), Wu & Faeth (1993), Faeth et al. (1995), Tsouris & Tavlarides (1994), and Luo & Svendsen (1996)]

$$\frac{L_{\rm H}}{L} \sim \left(\frac{2\pi\sigma}{\rho_l g L^2}\right)^{3/5} = We_L^{-3/5}.$$
 (2.4)

This is analogous to the well-known expression for the nondimensional Kolmogorov length scale $L_{\rm K}/L \sim Re_L^{-3/4}$, at which inertial and viscous effects are approximately balanced and $Re_{L_n} = Re_{L_{\rm K}} \sim 1$, where Re_{L_n} refers to the Reynolds number associated with u_{L_n} and L_n

$$Re_{L_n} = \frac{\rho_l u_{L_n} L_n}{\mu_l}. (2.5)$$

Recall Hinze's assumption that viscous effects are not dominant throughout the fragmentation cascade. This demands that the ratio $L_{\rm H}/L_{\rm K}\sim We_L^{-3/5}Re_L^{3/4}$ be large. For the breaking wave simulation considered here, $L_{\rm H}/L_{\rm K}\approx 100$, so the assumption is justified. Alternatively, one may write this ratio as

$$\frac{L_{\rm H}}{L_{\rm K}} \sim \left(\frac{\sigma}{\mu_l u_{L_{\rm K}}}\right)^{3/5}.\tag{2.6}$$

For air-water systems, the Kolmogorov velocity $u_{L_{\rm K}}$ will need to be larger than $\sigma/\mu_l \sim 10^2$ m/s in order for $L_{\rm K}$ to exceed $L_{\rm H}$. Thus, this assumption is satisfied for most terrestrial oceanic systems.

3. Bubble size distribution in breaking waves

Using the substantial mass test grouping criterion (Scheme C with $\phi_{c,m}=0.5$) in the flood-fill algorithm described in the companion brief (Chan et al. 2018b), the bubble size distribution was computed for the ensemble of breaking wave simulations described in Section 2. Using the timescale $T=\sqrt{g/L}$ such that the first impact occurs just after $t^*=t/T=1$, the ensemble-averaged bubble size distribution is plotted from $t^*=2.5$ at intervals of approximately $\Delta t^*=0.5$ in Figure 1. The nondimensional minimum grid spacing and the estimate for the nondimensional Hinze scale given by Eq. (2.4) are also

included in the plots in Figure 1. The effective size of nonspherical bubbles is computed by measuring the size of a spherical bubble of equal volume. A direct comparison of the evolution of the distribution with the corresponding wave structures from one of the ensemble members was performed by Chan et al. (2018a) and will not be repeated here. A numerical experiment to increase the nondimensional Hinze scale, keeping the nondimensional grid spacing constant, was also performed by Chan et al. (2018a) and will also not be revisited here.

Some key observations are listed here. First, a -10/3 power law initially develops in the size distribution above the Hinze scale, and momentarily extends into the sub-Hinzescale region around 2.8 $\lesssim t^* \lesssim$ 3.0. This scaling persists above the Hinze scale until about $t^* = 4.0$. These observations are consistent with the dominance of quasi-steady breakup by the action of turbulent eddies (Garrett et al. 2000) at scales both smaller and larger than the Hinze scale around $2.8 \lesssim t^* \lesssim 3.0$, and at scales larger than the Hinze scale before and after that, keeping in mind that the expression for the Hinze scale in Eq. (2.4) is merely an order-of-magnitude estimate. At early times, the signature of the turbulent cascade in the bubble size distribution is present only at the large scales because air is being entrained and fragmented from the large scales; at late times, turbulent breakup persists at the large scales as the smallest eddies in the system have the fastest timescales and disappear most quickly. Second, a -3/2 power law eventually develops below the Hinze scale at $t^* = 4.0$, and persists beyond $t^* = 5.1$. Note that this power-law scaling occurs fairly close to the grid scale. Third, a -4 power law is somewhat visible at intermediate sizes after $t^* = 4.0$. The two power-law fits that emerge at $t^* = 4.0$ (-3/2 for the small scales and -10/3 for the large scales) corroborate the experimental observations of Deane & Stokes (2002). A -4.36 power law was observed for what was postulated to be the super-Hinze-scale bubbles in a statistically-stationary set of measurements from air entrainment in a turbulent ship hull boundary layer (Masnadi et al. 2018), lending credence to the steeper power-law fit observed at large scales and at later times in this work where the role of buoyancy is expected to be more pronounced (than at earlier times). The replacement of the -10/3 power-law scaling by other power-law scalings in the size distribution, first at the small scales and then at the large scales, appears to be concurrent with the decay of turbulence, which is also expected to occur first at the small scales and then at the large scales. The apparent emergence of these new scalings following the dissipation of turbulence may be caused by the eventual development of a cascading process from small scales to large scales. The flow of air from small scales to large is reminiscent of coalescence processes, and motivates a deeper analysis of the driving of these processes by the background flow field with and without turbulence.

In light of the aforementioned evolution of the bubble size distribution—in particular, the observed power-law scalings—over the handful of characteristic times that make up the active wave-breaking period, one is motivated to examine the dynamics of the size distribution more rigorously. In the next section, an introduction to the population balance equation is provided in order to interpret the dynamics of the size distribution in relation to breakup and coalescence events.

4. Population balance equation

4.1. Formulation of the population balance equation

Consider the bubble size distribution $f(D; \vec{x}, t)$, defined as the number of bubbles of a certain effective size D per size interval at a given location in space \vec{x} per unit volume

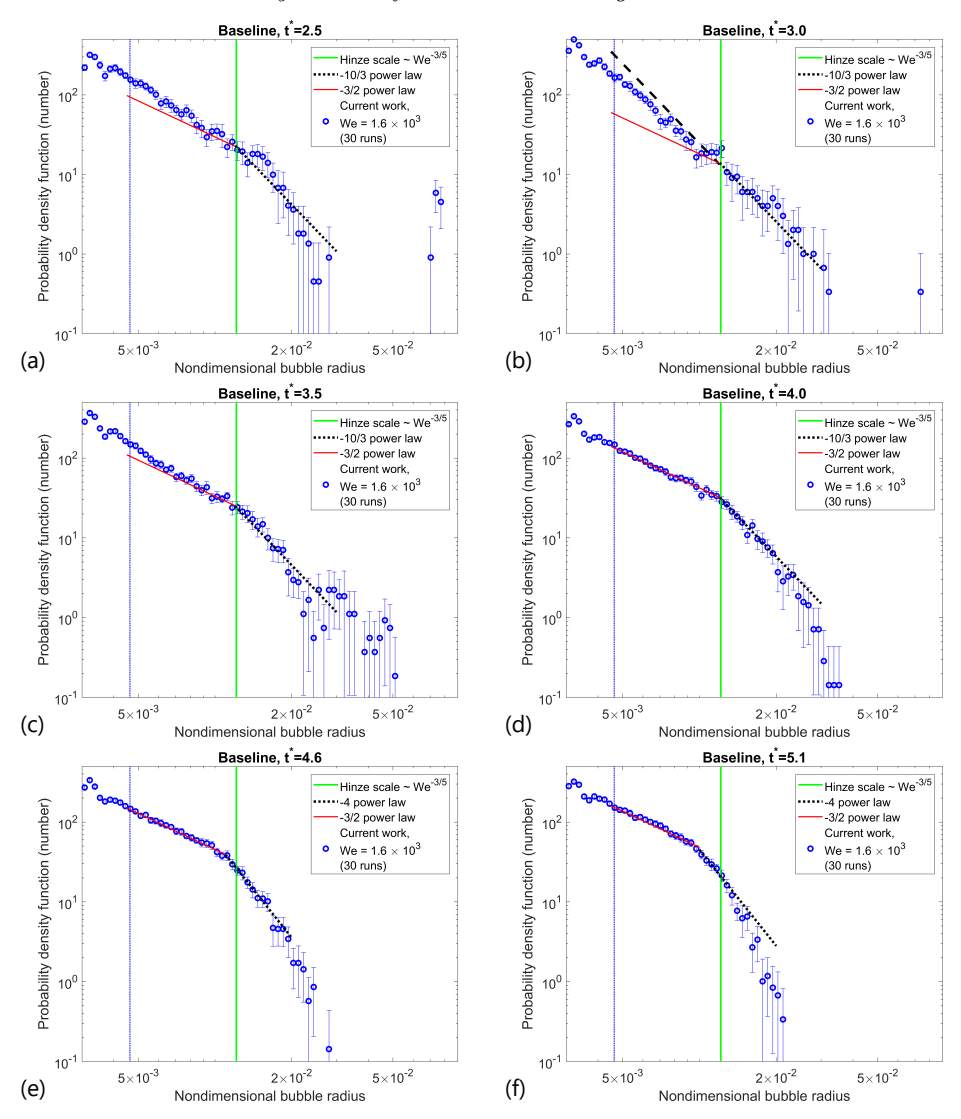


FIGURE 1. Ensemble-averaged bubble size distributions from 30 simulations of a breaking Stokes wave [every 85,000 time steps beginning at $t^* = 2.5$, increasing in time from (a) to (f)]. Wave parameters are detailed in Section 2. The dotted vertical line to the left denotes the grid resolution, while the solid vertical line to the right denotes the estimated Hinze scale given by Eq. (2.4). The solid sloped line to the left of the solid vertical line denotes a -3/2 power-law fit, while the dotted sloped line to the right of the solid vertical line denotes a -10/3 power-law fit in the first two rows and a -4 power-law fit in the last row. The error bars denote the 95% confidence interval over the ensemble for each bubble size bin.

and at a given time t. The dimensions of f are (length)⁻⁴. f may be computed via ensemble averaging over statistically-independent experimental or numerical runs of the same setup, in the limit of an infinite number of ensemble members. In the absence of dissolution and other mass transfer processes, one may phenomenologically construct a population balance equation describing the evolution of f (Williams 1958; Hulburt & Katz 1964; Valentas & Amundson 1966; Ramkrishna 1985; Williams 1985; Martínez-

Bazán et al. 1999)

$$\frac{\partial f}{\partial t} + \nabla_{\vec{x}} \cdot (\vec{u}f) = S_b + S_c. \tag{4.1}$$

Here, $\vec{u}(D; \vec{x}, t)$ is the mean velocity of all the bubbles of effective size D at the location \vec{x} and time t, and S_b and S_c are the rates of change of $f(D; \vec{x}, t)$ due to breakup and coalescence processes, respectively. Note that S_b and S_c may involve nonlocal fluxes in size space such that the component fluxes transfer bubbles across a noninfinitesimal size range (i.e., cause bubbles to undergo significant changes in size). If the system is homogeneous in space, then one may simplify the equation above to

$$\frac{\partial f}{\partial t} = S_b + S_c,\tag{4.2}$$

where f = f(D;t) describes the number of bubbles of effective size D per unit volume per size interval at a given time t averaged over all homogeneous directions. One may also interpret Eq. (4.2) as the outcome of integrating Eq. (4.1) over the physical domain of interest, assuming that the spatial boundary fluxes of f go to zero at the boundaries, or that they cancel each other out at appropriate boundary pairs due to homogeneity or periodicity. In other words, Eq. (4.2) is the volume-averaged equivalent of Eq. (4.1).

4.2. Breakup and coalescence fluxes in size space

The forcing terms S_b and S_c in Eq. (4.2) may each be expanded into a source flux and a sink flux. Assuming only binary breakup events occur, the breakup flux may be written as

$$S_b(D) = 2 \int_D^\infty q_b(D|D_p) g_b(D_p) f(D_p) dD_p - g_b(D) f(D),$$
 (4.3)

where $q_b(D|D_p)$ is the probability that a bubble of size D_p breaks into a bubble of size D (and another bubble such that the total volume remains constant), and $g_b(D)$ is the breakup frequency of a bubble of size D. Observe that $g_b(D)$ has dimensions (time)⁻¹, and may be computed, after volume averaging over each ensemble member, as follows

$$g_b(D) = \frac{\text{\# breakup events for bubbles of size } D \text{ per unit time per unit volume (vol.)}}{\text{\# bubbles of size } D \text{ per unit vol.}}$$
 (4.4)

When turbulent breakup is dominant $(D \gg L_{\rm H})$, it has been postulated on theoretical grounds (Coulaloglou & Tavlarides 1977) and confirmed experimentally with a refined theoretical model (Martínez-Bazán et al. 1999) that $g_b \sim D^{-2/3}$. One may obtain this relation from Eq. (2.2) by assuming that a bubble is most likely acted upon by a turbulent eddy of the same size, and thus that the breakup time of the bubble is of the same order as the turnover time of the eddy. Next, assuming only binary coalescence events occur, the coalescence flux may be written as

$$S_{c}(D) = \frac{1}{2} \int_{0}^{D} \int_{0}^{D} f(D_{1}) f(D_{2}) q_{c}(D_{1}, D_{2}) h(D_{1}, D_{2}) \delta\left(D - \sqrt[3]{D_{1}^{3} + D_{2}^{3}}\right) dD_{1} dD_{2}$$
$$-f(D) \int_{0}^{\infty} f(D_{p}) q_{c}(D, D_{p}) h(D, D_{p}) dD_{p},$$

$$(4.5)$$

where $q_c(D_1, D_2)$ is the probability that a bubble of size D_1 coalesces with a bubble of size D_2 given that they have collided, or the coalescence efficiency, and $h(D_1, D_2)$ is the frequency of collision events involving bubbles of sizes D_1 and D_2 . Note that the

coalescence efficiency q_c represents the likelihood that two bubbles of two particular sizes eventually coalesce after they come into contact, instead of bouncing apart. It is a function of the curvatures of the two interacting surfaces ($\sim 1/D_1$ and $1/D_2$), as well as the characteristic relative velocity between the two surfaces, which may also be modeled as a function of the two curvatures [see, also, the discussion of the coalescence of two liquid bodies by Chan et al. (2016, 2018a)]. In a numerical scheme where each computational cell (or node) may contain at most one phase interface, and the orientation of each interface depends on the orientation of the interfaces in the neighboring cells, two liquid or gas bodies will numerically coalesce once they come within one grid-cell width of each other. Thus, in the absence of artificial repulsive forces or subgrid-scale modeling, the effective numerical q_c should be taken as 1 when the model adopted for h is adequate. One may follow the kinetic-theory-based arguments put forward by Coulaloglou & Tavlarides (1977) and Prince & Blanch (1990) in order to write h(D) as $\delta u(D_1, D_2)A(D_1, D_2)$, where $A \sim (D_1 + D_2)^2$ is the collision cross section. Could glou & Taylarides assumed $\delta u \sim (u_1^2 + u_2^2)^{1/2}$ is the characteristic relative velocity between two particles of sizes D_1 and D_2 moving at characteristic speeds u_1 and u_2 . In general, $u_i \sim D_i^{\beta}$. In a fashion similar to the sink term in S_b , one may write the source term in S_c as

$$S_{c,+}(D) = \frac{1}{2} \int_0^D \int_0^D f(D_1) f(D_2) q_c(D_1, D_2) h(D_1, D_2) \delta\left(D - \sqrt[3]{D_1^3 + D_2^3}\right) dD_1 dD_2$$

$$\equiv g_c(D) f(D),$$

where $g_c(D)$ may be computed, also after volume averaging over each ensemble member, as follows

$$g_c(D) = \frac{\text{\# coalescence events creating bubbles of size } D \text{ per unit time per unit vol.}}{\text{\# bubbles of size } D \text{ per unit vol.}}$$
 (4.6

Note that g_c is not a quantity whose physical significance is immediately evident since the number of coalescence events creating bubbles of size D should not depend on the number density of bubbles of size D. Nevertheless, it is straightforward to measure numerically, and its scaling with D may be of interest.

4.3. Most favorable size ratio for coalescence events

Suppose turbulent breakup of large air cavities early in the flow generates bubbles whose size distribution momentarily follows a -10/3 power law in some size range. What is the size ratio that favors coalescence the most given this initial size distribution of bubbles? Suppose a bubble of size D is formed from the coalescence of bubbles of sizes D_1 and D_2 within this size range. Then, $D_1^3 + D_2^3 = D^3$ by the conservation of mass. If $r = D_2/D_1 > 1$, then $r = (D^3/D_1^3 - 1)^{1/3}$. The coalescence source flux may then be written as

$$S_{c,+} \sim f(D_1) f(D_2) \delta u(D_1, D_2) A(D_1, D_2)$$

$$\sim D_1^{-10/3} \left(D_1^{-10/3} r^{-10/3} \right) \left(D_1^{2\beta} + D_1^{2\beta} r^{2\beta} \right)^{1/2} (D_1 + D_1 r)^2$$

$$\sim D_1^{-14/3 + \beta} r^{-10/3} \left(1 + r^{2\beta} \right)^{1/2} (1 + r)^2. \tag{4.7}$$

It may be shown, for the conditions of interest, that this flux is maximized when $r \to \infty$. In other words, large-size-ratio coalescence events (between a very small bubble and a very large bubble) are highly favored from a collisional standpoint. See Appendix A for a more detailed characterization of $S_{c,+}$.

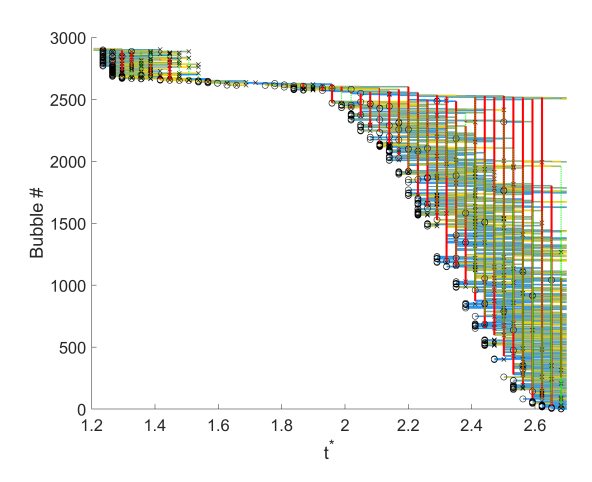


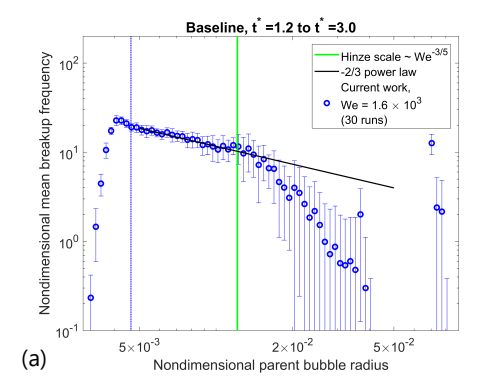
FIGURE 2. Family tree of bubbles constructed by the bubble tracking algorithm described by Chan et al. (2018b) for the breakup and coalescence of bubbles in one of the members of the simulation ensemble described in Section 2. The time interval between snapshots is $\Delta t^* = 0.03$. The bubble tags (vertical axis) are arbitrary. Each horizontal line depicts a bubble, and adopts a color between blue (largest bubble, darker in grayscale) and yellow (smallest bubble, lighter in grayscale) that is visible in the online version of this brief. Solid vertical lines (red in the online brief, thicker and darker in grayscale) depict breakup events, while dotted vertical lines (green in the online brief, thinner and lighter in grayscale) depict coalescence events. The colors of these lines are not essential to the interpretation of the tree for the purpose of this brief. Circles denote birth events and crosses denote death events. The significance of these events in a mass-conserving simulation with no inflow or outflow of air is discussed by Chan et al. (2018b).

5. Breakup and coalescence frequencies and probabilities

Using the bubble tracking algorithm described in the companion brief (Chan et al. 2018b), bubble breakup and coalescence events were identified in the simulation ensemble between $t^* = 1.2$ and $t^* = 4.8$. In a similar fashion to the last figure in the companion brief, Figure 2 illustrates what the timeline for these events looks like for one of the ensemble members between $t^* = 1.2$ and $t^* = 2.7$. The time interval between snapshots adopted in this work is $\Delta t^* = 0.03$. From Eqs. (2.2) and (2.3), one may estimate the minimum time interval required to capture, on average, the characteristic breakup frequency of bubbles at the Hinze scale $(\Delta t^*)_{\rm H} \sim 0.02$ for the wave considered in this work. One may also show, from these equations, that the breakup frequency corresponding to bubbles larger than the Hinze scale will be smaller (recall, from Section 4.2, that $g_b \sim D^{-2/3}$; thus, the time interval necessary to capture, on average, the breakup of these larger bubbles will be longer. The selected time interval between snapshots limits, on average, the maximum g_b that can be measured, which satisfies $g_{b,\max}\Delta t^* \sim 1$. Since the time interval selected in this work is on the same order as the minimum time interval estimated for the limiting case (Hinze scale), the maximum q_b that can be measured is close to the g_b expected at the Hinze scale, and work is ongoing to collect data with more frequent snapshots to better resolve this interval.

5.1. Breakup and coalescence frequencies

Figure 3 plots the ensemble-averaged and time-averaged breakup frequency g_b for the first and second halves of the duration of interest (1.2 < t^* < 3.0 and 3.0 < t^* < 4.8). At early times, a -2/3 power law is clearly observed for g_b over a wide range of scales,



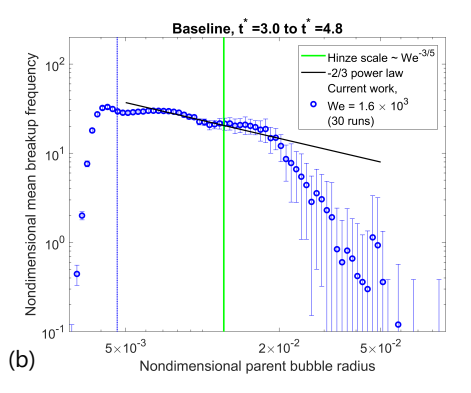
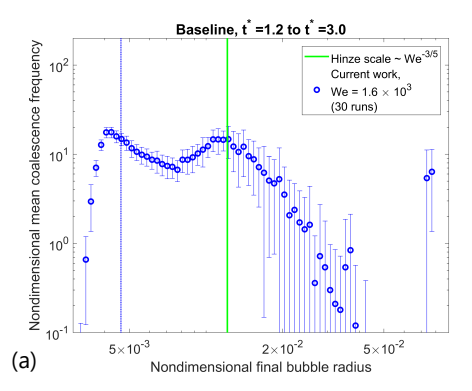


FIGURE 3. Breakup frequencies (g_b) for the simulation ensemble described in Section 2 for $1.2 < t^* < 3.0$ (a) and $3.0 < t^* < 4.8$ (b). A description of the vertical lines and error bars is provided in the caption of Figure 1. The sloped solid line depicts a -2/3 power-law fit.

suggesting the presence of a turbulent fragmentation cascade as discussed in Section 4. This is consistent with the -10/3 power law observed in the ensemble-averaged bubble size distribution in Figure 1. The -2/3 power-law fit for g_b is less adequate at later times $(t^* > 3.0)$, suggesting the cascade has largely ceased by then. Note that the -2/3power-law fit in Figure 3(a) does not extend completely into what was identified as the super-Hinze-scale region. There are a number of factors contributing to this peculiarity. First, super-Hinze-scale bubbles of different sizes are formed by the rupture of large air cavities, such as the cylindrical air cavity trapped when the wave overturns and breaks [see Figure 18 of Chan et al. (2018a)]. This means that the turbulent fragmentation cascade does not uniformly begin at a single scale, since each of these super-Hinze-scale seed bubbles generates its own fragmentation cascade from a different originating scale. Second, the statistics in Figure 3 are time-averaged. The number of super-Hinze-scale seed bubbles varies in time, from a negligible number before the large cavities have fragmented, to a significant number after this fragmentation has taken place, and again to a negligible number once these seed bubbles have fragmented and no new seed bubbles are generated to take their place. This variation in the number of super-Hinze-scale seed bubbles may obfuscate the interpretation of the breakup frequency at these large scales. Mathematically, one should note that $\int g_h dt \neq (\int f g_h dt)/(\int f dt)$. As remarked in the companion brief (Chan et al. 2018b), ensemble averaging is the proper way to take statistics in a statistically-unsteady flow, and work is ongoing to collect more converged statistics after reducing the averaging time window for these events in an attempt to move towards ensemble averaging. Third, the turbulence in the continuous phase may be sufficiently modulated at these large scales by the presence of the dispersed phase.

Figure 4 plots the ensemble-averaged and time-averaged coalescence frequency g_c for the first and second halves of the duration of interest $(1.2 < t^* < 3.0 \text{ and } 3.0 < t^* < 4.8)$. The coalescence frequency peaks close to the estimated Hinze scale, and work is ongoing to determine the physical significance of this observation. Coalescence is potentially inhibited at large scales where the effects of turbulence prevent imminent collisions from going to completion [see, e.g., the discussions by Shinnar & Church (1960), Shinnar (1961) and Church & Shinnar (1961) for droplets, and Prince & Blanch (1990) for bubbles, which model this inhibition in q_c when the kinetic theory model for h is maintained]. In addition, the variation of the coalescence frequency with bubble size differs in both time intervals, suggesting that the nature of the background flow inducing the coalescence



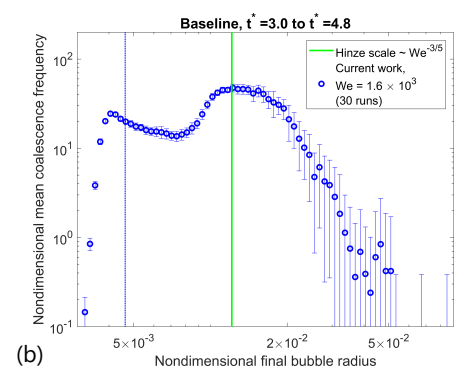


FIGURE 4. Coalescence frequencies (g_c) for the simulation ensemble described in Section 2 for $1.2 < t^* < 3.0$ (a) and $3.0 < t^* < 4.8$ (b). A description of the vertical lines and error bars is provided in the caption of Figure 1.

cence of bubbles is different in both time intervals. A more precise characterization of the background flow in these time intervals is in progress.

5.2. Breakup and coalescence probabilities

Before analyzing the probability distributions of the relative sizes of the final (breakup) / initial (coalescence) bubbles involved in these breakup and coalescence events, it is instructive to divide the size range of observable bubbles into three distinct phenomenologies: resolved small bubbles (sub-Hinze-scale bubbles with nondimensional radii 6 \times $10^{-3} < r^* = r/L < 1.2 \times 10^{-2}$), large bubbles (super-Hinze-scale bubbles, $1.2 \times 10^{-2} < 10^{-2}$ $r^* < 3 \times 10^{-2}$) and very large "bubbles" (super-Hinze-scale air cavities, $r^* > 3 \times 10^{-2}$). This enables a more targeted analysis of the various breakup and coalescence events. In addition, the subsequent figure will analyze the occurrence of these events as a function of the volume ratio of the constituent bubbles. The bubble volume ratio distribution for breakup events corresponds to q_h . For breakup events, the volume of each of the two descendant (child) bubbles as a ratio of the sum of the volumes of these bubbles is of interest. For coalescence events, the volume of each of the two ancestor (parent) bubbles as a ratio of the sum of the volumes of these bubbles is of interest. In the case of the latter, the simulation ensemble inherently requires that all bubble pairs that come into contact undergo successful coalescence since the grid resolution of these simulations does not permit accurate temporal and spatial resolution of coalescence events. In other words, the coalescence events accounted for here include physical and numerical coalescence, and the effective q_c for most of these events is 1 provided h is modeled adequately.

Figure 5 plots the statistics of the breakup and coalescence events where the ancestor (breakup) / descendant (coalescence) bubble belongs to the category of large bubbles. The breakup distribution indicates that breakup generates bubble pairs of a broad range of size ratios. The coalescence distribution indicates that large-size-ratio coalescence events are favored. This supports the kinetic theory framework explored in Sections 4.2 and 4.3, and motivates the need to accurately capture large-size-ratio events in the bubble tracking algorithm (Chan et al. 2018b). Note that coalescence events where the smaller ancestor bubble has a nondimensional radius $r^* < 6 \times 10^{-3}$ have not been included in Figure 5. If these events are included, the bias in the distribution towards large-size-ratio events will be more significant. From both distributions, it appears that the number of coalescence events is on the same order as the number of breakup events, suggesting that

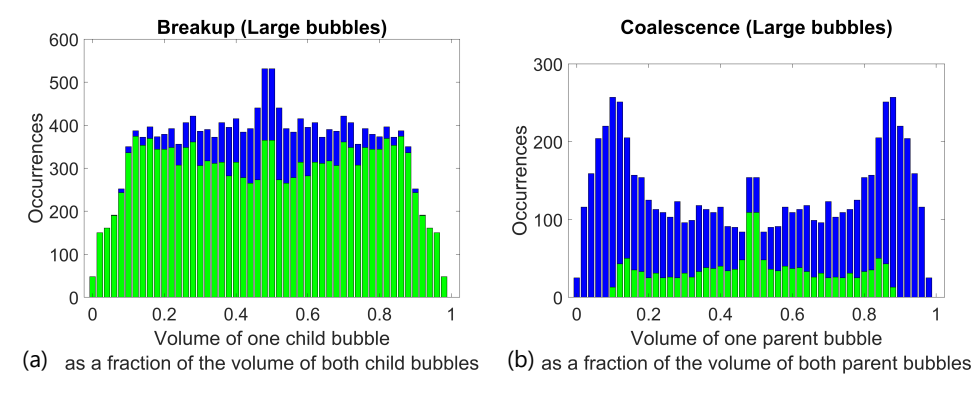


FIGURE 5. Conditional bubble volume ratio distributions due to some of the breakup (a) and coalescence (b) events in the simulation ensemble described in Section 2. For breakup, events where the ancestor bubble is a large bubble (super-Hinze-scale bubble) and both descendant bubbles have nondimensional radii $r^* > 6 \times 10^{-3}$ are included. The distribution is divided into two groups. The top portion of each bar (blue in color, darker in grayscale) denotes events where the smaller of the two descendant bubbles is a large bubble. The bottom portion (green in color, lighter in grayscale) denotes events where the smaller of the two descendant bubbles is a resolved small bubble (sub-Hinze-scale bubble). For coalescence, events where the descendant bubble is a large bubble and both ancestor bubbles have nondimensional radii $r^* > 6 \times 10^{-3}$ are included. The top (blue/darker) portion of each bar denotes events where the larger of the two ancestor bubbles is a large bubble. The bottom (green/lighter) portion denotes events where the larger of the two ancestor bubbles is a resolved small bubble.

breakup and coalescence events have comparable impact on the dynamics of the bubble size distribution in breaking waves, in contrast to what Hinze (1955) postulated in the derivation of the Hinze scale. Because these events dominate at different stages of the flow, the resultant distributions evolve in time in a rich manner. In addition, unity-size-ratio events involving bubbles of almost equal sizes appear to be favored in both breakup and coalescence. The physical significance of this trend is also being examined.

6. Conclusions

The bubble identification and tracking algorithms outlined in the companion brief (Chan et al. 2018b) are used to compute and analyze the bubble size distribution resulting from an ensemble of simulations of breaking Stokes waves. The distribution is compatible with a turbulent breakup mechanism at early times, and shifts, first at the small scales and then at the large scales, at later times. This evolution of the bubble size distribution is further analyzed within a population balance equation-based framework that accounts for transfer fluxes in size space due to breakup and coalescence events. Breakup and coalescence frequencies and probabilities are computed directly from the simulation ensemble to provide insights into the population dynamics. The breakup frequencies support the turbulent breakup mechanism, and large-size-ratio coalescence events observed in the simulations support a kinetic-theory-based approach for describing and modeling coalescence. Based on the observations collected from these tools, a potential sequence of events governing the evolution of the bubbles is proposed as follows: as the wave breaks, turbulent fragmentation of large air cavities generates smaller bubbles of a wide range of sizes. A -10/3 power-law size distribution is generated by this turbulent fragmentation. Even though typical derivations of this power-law fit neglect the effects of coalescence, evidence suggests that coalescence events may occur as frequently as breakup events in

these flows, if not more. Subsequently, after the turbulence has mostly dissipated and ceased to exist, a -3/2 power-law scaling develops in the size distribution for bubbles smaller than what was formerly the Hinze scale—the Hinze scale is no longer a relevant measure when the turbulence has mostly ceased to exist—and bubbles of intermediate size begin to conform to a -4 power-law size distribution. Because the power-law scaling at the small scales changes first, and then the scaling at the large scales, a coalescence cascade from small scales to large scales could be developing late in the wave-breaking process. Work is ongoing to identify the locations and corresponding features in the flow where some of these breakup and coalescence events are occurring, in order to ascertain the mechanisms generating these events and better model the characteristic length, time, and velocity scales involved. Additional analysis of the breakup and coalescence statistics is also under way to strengthen their connection with the model population dynamics. In particular, derivation of more detailed models and scaling relations for g_b , g_c , q_b , q_c and h is under way, and the relevant physical processes in the background flow contributing to these breakup and coalescence events will hopefully be elucidated in the process.

As mentioned in the companion brief, a fundamental understanding of breakup and coalescence processes that govern the formation and evolution of bubbles in breaking waves may assist in developing subgrid-scale (SGS) models for turbulent bubbly flows. In light of the observations above, a preliminary SGS model for the largest sub-Hinzescale bubbles is proposed as follows: at early times, poorly resolved bubbles should be broken up into subgrid Lagrangian bubbles with frequency g_b as if they were subject to a turbulent fragmentation cascade that extends into the subgrid scales. Although not directly investigated in this work, satellite bubbles are also expected from bubble pinchoff events near the neck connecting the child bubbles (Gordillo & Fontelos 2007) and may be modeled with capillary instability theory in tandem with the film bubbles discussed by Chan et al. (2016, 2017, 2018a) and Mirjalili & Mani (2018). Coalescence models for these subgrid Lagrangian bubbles will be necessary, and a more fundamental understanding of the coalescence mechanisms in these waves will inform the development of these models. Because large-size-ratio collisions between bubbles are favored, coalescence is expected between pairs of subgrid bubbles, as well as between bubble pairs comprising one subgrid bubble and one resolved bubble. These coalescence models will need to handle both subgrid bubble-subgrid bubble and subgrid bubble-resolved bubble coalescence events.

Acknowledgments

This investigation was funded by the Office of Naval Research, Grant #N00014-15-1-2726. W. H. R. Chan is also funded by a National Science Scholarship from the Agency of Science, Technology and Research in Singapore. The authors acknowledge computational resources from the U.S. Department of Energy, as well as from the Certainty cluster awarded by the National Science Foundation to CTR. The authors are grateful to Prof. Ali Mani for fruitful discussions regarding physical interpretation and presentation of the breakup and coalescence probabilities.

Appendix A. Conditions for monotonicity of the coalescence source flux $S_{c,+}$

Here, the conditions under which $S_{c,+}$ is monotonically decreasing are elaborated upon. Recall the following expression for $S_{c,+}$

$$S_{c,+} \sim D_1^{-14/3+\beta} r^{-10/3} \left(1 + r^{2\beta}\right)^{1/2} (1+r)^2.$$
 (A1)

Note that the only free parameter in this problem is $s = D_1/D$, where $0 < s < 1/\sqrt[3]{2}$. r may then be expressed in terms of s as $r = (s^{-3} - 1)^{1/3}$. Substituting this into Eq. (A 1) yields

$$S_{c,+} \sim s^{-14/3+\beta} r^{-10/3} (1+r^{2\beta})^{1/2} (1+r)^2 D^{-14/3+\beta}$$

It may be graphically verified for an initial -10/3 power-law bubble size distribution and $|\beta| \sim O(1)$ that $S_{c,+}$ is a monotonically decreasing function of s, suggesting in these cases that large-size-ratio coalescence events are highly favored from a collisional standpoint when the number density of small bubbles sufficiently exceeds the number density of large bubbles. It was observed that the range of β for which this monotonic trend is present increases as the power law becomes steeper (i.e., if $f \sim D^{\gamma}$ and $\gamma < 0$, then as the magnitude of γ increases). More generally, the range of validity of this monotonic variation in $S_{c,+}$ in the parameter space $\{\beta,\gamma\}$ may be derived by enforcing $\partial S_{c,+}/\partial s < 0$ for $0 < s < 1/\sqrt[3]{2}$, and the resulting constraint is

$$(2\gamma + \beta + 2)r^3s^3 - \gamma - \beta r^{2\beta}/(1 + r^{2\beta}) - 2r/(1 + r) < 0.$$

REFERENCES

- BLENKINSOPP, C. E. & CHAPLIN, J. R. 2010 Bubble size measurements in breaking waves using optical fiber phase detection probes. *IEEE J. Ocean Eng.* **35**, 388–401.
- Chan, W. H. R., Urzay, J., Mani, A. & Moin, P. 2016 On the development of a subgrid-scale model for the generation of micro-bubbles from impacting liquid surfaces. *Annual Research Briefs*, Center for Turbulence Research, Stanford University, pp. 149–162.
- Chan, W. H. R., Urzay, J. & Moin, P. 2017 Development of a collision detection algorithm for complex two-phase flows. *Annual Research Briefs*, Center for Turbulence Research, Stanford University, pp. 103–116.
- Chan, W. H. R., Urzay, J. & Moin, P. 2018a Subgrid-scale modeling for microbubble generation amid colliding water surfaces. *Proceedings of the 32nd Symposium on Naval Hydrodynamics*, Hamburg, Germany.
- Chan, W. H. R., Dodd, M. S., Johnson, P. L., Urzay, J. & Moin, P. 2018b Formation and dynamics of bubbles in breaking waves: Part I. Algorithms for the identification of bubbles and breakup/coalescence events. *Annual Research Briefs*, Center for Turbulence Research, Stanford University, pp. 3–20.
- Church, J. M. & Shinnar, R. 1961 Stabilizing liquid-liquid dispersions by agitation. *Ind. Eng. Chem.* **53**, 479–484.
- Coulaloglou, C. A. & Tavlarides, L. L. 1977 Description of interaction processes in agitated liquid-liquid dispersions. *Chem. Eng. Sci.* **32**, 1289–1297.
- Deane, G. B. & Stokes, M. D. 2002 Scale dependence of bubble creation mechanisms in breaking waves. *Nature* 418, 839–844.
- Deike, L., Melville, W. K. & Popinet, S. 2016 Air entrainment and bubble statistics in breaking waves. *J. Fluid Mech.* **801**, 91–129.
- FAETH, G. M., HSIANG, L.-P. & Wu, P.-K. 1995 Structure and breakup properties of sprays. *Int. J. Multiphas. Flow* 21, 99–127.
- GARRETT, C., LI, M. & FARMER, D. 2000 The connection between bubble size spectra and energy dissipation rates in the upper ocean. J. Phys. Oceanogr. 30, 2163–2171.

- GORDILLO, J. M. & FONTELOS, M. A. 2007 Satellites in the inviscid breakup of bubbles. *Phys. Rev. Lett.* **98**, 144503.
- HINZE, J. O. 1955 Fundamentals of the hydrodynamic mechanism of splitting in dispersion processes. *AIChE J.* 1, 289–295.
- HULBURT, H. M. & KATZ, S. 1964 Some problems in particle technology: a statistical mechanical formulation. *Chem. Eng. Sci.* **19**, 555–574.
- IAFRATI, A. 2009 Numerical study of the effects of the breaking intensity on wave breaking flows. J. Fluid Mech. 622, 371–411.
- KIM, D., HAM, F., BOSE, S., LE, H., HERRMANN, M., LI, X., SOTERIOU, M. C. & KIM, W. High-fidelity simulation of atomization in a gas turbine injector high shear nozzle. *ILASS Americas 26th Annual Conference*, Portland, OR, USA, May 2014.
- Kolmogorov, A. N. 1941 The local structure of turbulence in incompressible viscous fluid for very large Reynolds numbers. *Dokl. Akad. Nauk SSSR* **30**, 299–303.
- KOLMOGOROV, A. N. 1949 On the breakage of drops in a turbulent flow. *Dokl. Akad. Nauk SSSR* **66**, 825–828.
- Kolmogorov, A. N. 1962 A refinement of previous hypotheses concerning the local structure of turublence in a viscous incompressible fluid at high Reynolds number. J. Fluid Mech. 13, 82–85.
- Luo, H. & Svendsen, H. F. 1996 Theoretical model for drop and bubble breakup in turbulent dispersions. *AIChE J.* 42, 1225–1233.
- Martínez-Bazán, C., Montañés, J. L. & Lasheras, J. C. 1999 On the breakup of an air bubble injected into a fully developed turbulent flow. Part 1. Breakup frequency. J. Fluid Mech. 401, 157–182.
- MASNADI, N., ERININ, M. A., WASHUTA, N., NASIRI, F., BALARAS, E. & DUNCAN, J. H. 2018 Air entrainment and surface fluctuations in a turbulent ship hull boundary layer. *Proceedings of the 32nd Symposium on Naval Hydrodynamics*, Hamburg, Germany.
- MIRJALILI, S. & MANI, A. 2018 High fidelity simulations of micro-bubble shedding from retracting thin gas films in the context of liquid-liquid impact. *Proceedings of the 32nd Symposium on Naval Hydrodynamics*, Hamburg, Germany.
- PRINCE, M. J. & BLANCH, H. W. 1990 Bubble coalescence and break-up in air-sparged bubble columns. $AIChE\ J.\ 36$, 1485–1499.
- RAMKRISHNA, D. 1985 The status of population balances. Rev. Chem. Eng. 3, 49–95.
- SHINNAR, R. & CHURCH, J. M. 1960 Statistical theories of turbulence in predicting particle size in agitated dispersions. *Ind. Eng. Chem.* **52**, 253–256.
- Shinnar, R. 1961 On the behaviour of liquid dispersions in mixing vessels. *J. Fluid Mech.* 10, 259–275.
- TSOURIS, C. & TAVLARIDES, L. L. 1994 Breakage and coalescence models for drops in turbulent dispersions. *AIChE J.* **40**, 395–406.
- Valentas, K. J. & Amundson, N. R. 1966 Breakage and coalescence in dispersed phase systems. *Ind. Eng. Chem. Fund.* **5**, 533–542.
- Wang, Z., Yang, J. & Stern, F. 2016 High-fidelity simulations of bubble, droplet and spray formation in breaking waves. *J. Fluid Mech.* **792**, 307–327.
- WILLIAMS, F. A. 1958 Spray combustion and atomization. Phys. Fluids 1, 541–545.
- Williams, F. A. 1985 Combustion Theory. Addison-Wesley.
- Wu, P.-K. & Faeth, G. M. 1993 Aerodynamic effects on primary breakup of turbulent liquids. *AIAA Paper* 93-0903.